

Contents lists available at ScienceDirect

Fuel

journal homepage: www.elsevier.com/locate/fuel



Full Length Article

Quantitative investigation of sooting dynamics in droplet combustion using an automated image analysis algorithm

Yuhao Xu^{a,1,*}, Yiren Shen^b, C. Thomas Avedisian^{b,*}, Michael C. Hicks^c, Mun Y. Choi^d

- a Department of Mechanical Engineering, Prairie View A&M University, Prairie View, TX 77446, USA
- ^b Sibley School of Mechanical and Aerospace Engineering, Cornell University, Ithaca, NY 14853, USA
- ^c NASA-Glenn Research Center, Combustion and Reacting Systems Branch, 21000 Brookpark Road, Cleveland, OH 44135, USA
- ^d Department of Mechanical and Aerospace Engineering, University of Missouri, Columbia, MO 65211, USA

ARTICLE INFO

Keywords: Droplet combustion n-Heptane Soot Image analysis Soot volume fraction Full field light extinction method

ABSTRACT

This paper reports an image analysis approach using a newly-developed open-source program to extract quantitative measurements of soot volume fraction (SVF) from digital video images of burning n-heptane droplets. The automated program developed in this work can analyze images of fixed and untethered droplets to quantify sooting dynamics. The images analyzed in the program were taken from experiments carried out in the Multi-user Droplet Combustion Apparatus (MDCA) onboard the International Space Station (ISS). In these experiments, video imaging of burning droplets was obtained using backlighting by a laser diode with a wavelength of 653 nm. The light was collimated before it passed through the droplet and soot-containing region, after which the light was then attenuated and projected onto the camera's sensors. This technique facilitates the measurements of SVF based on the principles of the full field light extinction method (FFLEM). The measurements provide quantitative data that reveal the sooting dynamics of liquid fuels during droplet combustion processes.

The analyses of a soot-attenuating image (ISS n-heptane, untethered droplet) at an instant during the burning show that the SVF distribution has a peak at the soot shell location. It then decreases due to soot oxidation when the location is further away from the burning droplet. Regarding temporal effects on the maximum SVF (SVF_{max}), results show that SVF_{max} first increases after the burning is initiated until a peak value is reached, after which SVF_{max} decreases. The SVF_{max} values identified in this study for n-heptane are quantitatively consistent with previously reported values for fiber-supported droplets and are reached relatively early in the burning history. n-Heptane images are also analyzed to show the effects of initial droplet sizes on the maximum soot volume fraction. Results show that SVF_{max} decreases with increasing initial droplet size, which is consistent with visual observations of less soot formed and dimmer flame brightness as D_0 increases.

1. Introduction

As an integral part of the combustion processes for many liquid fuel systems, sooting dynamics have received much attention due to their close relationship with radiant heat transport and post-flame particulate control [1]. The complexities of sooting dynamics in practical combustors, such as sprays, can be reduced by studying the combustion of isolated fuel droplets. When the gas transport around a burning fuel droplet is entirely driven by the evaporation process of the fuel without external flow influences, it results in a one-dimensional (1-D) burning configuration that is spherically symmetric. When soot particles form in this configuration, they will be positioned between the flame and the

droplet in a porous shell-like structure by a balance of forces acting on them: outwardly directed follow because of the fuel evaporation and inwardly directed thermophoresis. This spherically symmetric combustion configuration still links to sprays that set the initial conditions for combustion in engines [2], where the in-cylinder environment can include the presence of fuel droplets [3–6]. Moreover, the soot shell structure in this configuration will significantly facilitate the analyses of sooting behaviors during combustion.

The spherically symmetric gas transport and 1-D flow process are often promoted by carrying out experiments in microgravity environments. The removal of the convection effects and the resulting spherical symmetry provides an ideal condition for soot agglomerate observations [7]. Jackson et al. [8] observed the combustion of sooting fuel droplets

^{*} Corresponding authors.

E-mail addresses: yuhaox@clemson.edu (Y. Xu), cta2@cornell.edu (C.T. Avedisian).

¹ Current address: Department of Mechanical Engineering, Clemson University, Clemson, SC 29634, USA.

Nomenclature G			Greek Letters	
		κ	Attenuation coefficient	
D_{ik}	Operation coefficients for the three-point Abel inversion	λ	Wavelength of the laser light, m	
Do	Initial droplet diameter, mm, m, or pixel	θ	Direction-of-analysis angle	
f_{ν}	Soot volume fraction	$\rho_{\mathbf{p}}$	Pearson correlation coefficient	
$f_{\nu,j}$	Soot volume fraction of the j-th element	411 .		
$f_{\nu, ext{max}}$	Maximum soot volume fraction	Abbrevia		
I	Light intensity	ASI	Apparent Soot Index	
I_j	Incident light intensity of the j-th element	BW	Black-and-white	
I_{j+1}	Transmitted light intensity of the j-th element	CIR	Combustion Integrated Rack	
Io	Incident light intensity prior to the first element	DOA	Direction-of-analysis	
Ke	Extinction coefficient	DOE	Department of Energy	
L	Path length of the light beam, m	FFLEM	Full-field light extinction method	
L_j	Path length of the attenuated light in the j-th element, m	FLEX-2	Flame Extinguishment-2	
n	Number of the ray-of-interests under investigation	fps	Frames per second	
P	Line-of-sight projection data, m	HiBMs	High Bit-Depth Multispectral	
r	Projection of R onto the x-z plane; or radius, m	ISS	International Space Station	
$r_{\rm d}$	Radius of the droplet, m or pixel	LOS	Line-of-sight	
r _i	Radial distance from the center of the droplet on the x-z	MC	Monte Carlo	
	plane, m or pixel	MDCA	Multi-user Droplet Combustion Apparatus	
R	Direction of interest in the three-dimensional space	MP	Megapixel	
t	Time, s	ppm	Parts per million	
x	x-axis in the Cartesian coordinate system	ROI	Ray-of-interest	
у	y-axis in the Cartesian coordinate system; direction along	SSR	Soot Standoff Ratio	
	the light beam	SVF	Soot Volume Fraction	
z	z-axis in the Cartesian coordinate system			

under microgravity, using n-heptane, monochloroalkanes, and their mixtures, and discovered the effects of soot on droplet vaporization rates. The degree of sooting, however, was based on visual observation of the soot shell opacity, which reflected the relative sooting tendencies with constant backlighting [8,9]. Bae and Avedisian [10] proposed a semi-quantitative assessment of soot by defining an "apparent soot index" (ASI), a ratio of the darkest areas surrounding a droplet for JP8/TPGME blends relative to that of "pure" JP8. This ratio provided a more quantitative measurement of sooting behavior than purely visual observation. A more accurate measurement of the spatial distribution of soot formation in the combustion zone would benefit from inferring a three-dimensional distribution of soot from a two-dimensional image. Such a capability is presented in this paper to examine the soot volume fraction (SVF, f_{ν}), which reflects the volume fractions occupied by soot within the flame [11].

In droplet combustion studies, two diagnostic approaches for SVF measurement were favorably considered due to their nonintrusive nature: laser-induced incandescence (LII) and full-field light extinction method (FFLEM) [12]. LII uses photo-detectors to record the incandescence emitted from soot particles heated to their sublimation temperature by a short-duration, high-powered laser [13]. Vander Wal et al. [14] performed laser-induced incandescence measurements for relative soot concentration measurements of heptane and decane fuel droplets burning under normal-gravity conditions. Gupta et al. [15] also conducted soot volume fraction measurements with LII for methanol/benzene droplet flames. However, LII does not provide an absolute soot volume fraction and must be calibrated against other techniques [16]. Moreover, the high-intensity LII pulses can cause dramatic morphological changes and even mass loss to the soot particles. Another possible problem for LII is the significant signal trapping for heavily sooting flames [12].

The full-field light extinction technique can provide nonintrusive measurements for absolute soot volume fraction values [1]. This technique is based on the principle of light attenuation, which occurs when a laser beam passes through a spherically symmetric soot-containing region of the droplet flame. Soot volume fraction distribution is then

determined by an inversion process of the laser intensity attenuation through planar surfaces that are normal to the radial direction. Moreover, FFLEM experiments that are coupled with tomographic inversion techniques have the ability to examine the entire soot field instantaneously and thus can provide the absolute SVF distribution in droplet flames [17].

Choi and Lee [18] conducted the first FFLEM-based microgravity droplet combustion experiment using FFLEM-based nonintrusive soot measurements. The tomographic inversion technique involving Abel transforms was utilized to obtain the soot concentrations for microgravity heptane droplet flames. Lee et al. [19] later conducted a comprehensive study on the effects of initial diameter on sooting and burning behavior of isolated droplets under microgravity conditions. Manzello et al. [20] demonstrated, for the first time, that sooting tendency decreases with larger droplets, which were accompanied by higher burning rates under microgravity conditions. Manzello et al. [21] also investigated the soot shell formation mechanism in microgravity droplet combustion. Urban et al. [22] studied the sooting behavior of small ethanol droplets at higher ambient pressures and various oxygen indices in microgravity environments. Manzello et al. [23] performed microgravity combustion experiments on hexane, heptane, nonane, and decane droplets to investigate the fuel-dependent effects on droplet burning and sooting behaviors. They found the soot standoff ratio (SSR) for decane was significantly smaller than that of other fuels tested, while the flame standoff ratios (FSR) were of similar magnitude. In a recent study, Park and Choi [24] studied the effect of the residence time of fuel vapor transport on the sooting behavior of ethanol droplet flames under microgravity conditions.

Despite the continuous interest in sooting dynamics within the microgravity droplet combustion community, there is currently no open-source program available to extract soot volume fraction measurements from consecutive digital images [18–24]. In the present study, an automated sooting analysis program for both fixed and moving droplets is developed in MATLAB, which offers high-performance computation and visualization capabilities and various application development toolboxes [25]. The fuel system used in the present study is

n-heptane because of its relevance as a primary reference fuel component for gasoline and a constituent component of gasoline and jet fuels.

The innovations of this work can be categorized into three aspects. First, a detailed theoretical derivation of the method and its implementation are presented in this paper. Second, an open-source program is developed to automatically obtain SVF measurements from images recorded during droplet combustion experiments. The program can extract SVF data for untethered droplets during combustion. The program is applied to analyze experimental data from the International Space Station (ISS) experiments on burning droplets. During these experiments, droplets were untethered and can drift during a burn, and thus the new feature of automatically identifying the droplet center is critical to analyzing the images. Finally, this paper uses the data obtained from the newly developed automatic program to present the influences of initial droplet diameters (Do) on the SVF dynamics of nheptane droplet combustion. Results reported showcase the capability of the new program and also provide unique insights into the sooting dynamics of droplet combustion. Specifically, the effects of initial diameters and their temporal evolution on SVF are presented, covering a wide range of initial diameters (1.59 mm to 3.55 mm).

The next sections outline the experimental design and procedures, the theory of FFLEM, the newly developed "analyze_SVF" algorithm for SVF measurements, and a presentation of the results.

2. Description of the experiment

The data presented here are obtained from experiments performed onboard the International Space Station as part of the Flame Extinguishment-2 (FLEX-2) program, which focused on untethered droplet combustion experiments [26–28]. The images of *n*-heptane analyzed in this study were previously reported in Ref. [26], emphasizing the droplet and flame dynamics as the initial droplet diameters increased from half a millimeter to almost 5 mm, without much emphasis on the quantitative sooting information. In this work, the efforts have been focused on obtaining quantitative soot measurements, which will provide valuable data for detailed numerical modeling (DNM) of droplet combustion [28–30].

The Multi-user Droplet Combustion Apparatus (MDCA), integrated into the Combustion Integrated Rack (CIR), is used to perform experiments onboard the ISS. An outline of the experimental approach and procedures is discussed here, while detailed hardware descriptions are reported elsewhere [31–33].

The fuel droplets are formed by dispensing liquid fuel through two needles, which are separated by a small distance to create a liquid bridge. Once the desired droplet size is reached, the liquid bridge is slightly stretched to minimize the drift after droplet deployment. The two needles are then rapidly retracted with an untethered droplet left between two igniters. The fuel droplet is ignited by two hot wires that are energized after the needles are retracted. The igniters are then retracted after ignition to minimize the influence on the thermal field around the droplet, and the spherical droplet flame is thus obtained. The ambient environment is atmospheric pressure air at room temperature. The droplet burning process is recorded by a High Bit-Depth Multispectral (HiBMs) camera (1 MP at 30 fps) with a backlight source that facilitates the implementation of the FFLEM technique as discussed below. A color camera (0.3 MP at 30 fps) is also part of the hardware to provide self-illuminated flame images. The color flame images are not involved in the FFLEM method reported in this work but are mentioned for the completeness of the experimental hardware.

The backlit lighting for the HiBMs camera on MDCA onboard the ISS is provided by a laser diode with a wavelength of 653 nm. The light is collimated before passing through the droplet and the soot-containing region and then attenuated and projected onto the HiBMs camera sensors. This diagnostic technique facilitates soot volume fraction measurements using the full-field light extinction method.

3. Full-field light extinction method

Fig. 1 provides a schematic of the FFLEM, which is used to quantitatively obtain the SVF within the MDCA for the spherically symmetric droplet combustion configuration. The laser beam is collimated, and the parallel light travels through the soot-containing region that contains small particles. When light passes through a medium with small particles, the incident light beam is attenuated by absorption and scattering processes [34]. These two processes result in a combined attenuation of the light, called extinction. The attenuated light beam is projected onto the camera sensor that is orthogonal to the incident light and along the line-of-sight direction (LOS, i.e., y-direction in Fig. 1). With the condition of spherical symmetry, the recorded intensity on black-and-white (BW) images is radially symmetric to the center of the fuel droplet. Therefore, a ray-of-interest (ROI) can start from the center of the droplet to investigate the projected light intensity. The variation of the light intensity in the recorded images I(r), as a function of the radial direction r, is negatively related to the transmittance of the light beam through the soot-containing region. This projected light intensity data depend on the symmetric distribution of the SVF. Therefore, tomographic inversion techniques can be applied to reconstruct the spatial distribution of the SVF with light-intensity data on the BW images and other parameters related to the experimental setup, as discussed later. The main assumptions of this process include the symmetric field distribution [35], and soot particles are small, so the Mie theory is applicable [36].

The so-called line-of-sight projection data, P(r), is a mathematical parameter that can be expressed as the integration of the field distribution of SVF [35]:

$$P(r) = \int_{-\infty}^{\infty} f_{\nu}(R) \, dy = \int_{-\infty}^{\infty} f_{\nu}\left(\sqrt{r^2 + y^2}\right) \, dy, \tag{1}$$

where R is a direction of interest in the three-dimensional space, r is the projection of R onto the x-z plane (i.e., the same plane of the camera sensor and thus the BW images), y is the direction along the light beam, and f_v is the soot volume fraction. Fig. 2 presents the coordinate system related to Equation (1) to better illustrate the relationship between R and r.

To perform the tomographic inversion and thus calculate the soot volume fraction, the value of P in Equation (1) is needed. Discretization in both y- and z-directions, as shown in Fig. 3, facilitates the process of obtaining a mathematical expression for P. We use m (i.e., $k=1,2,3\ldots$ m) and n (i.e., $j=1,2,3\ldots$ n) elements to represent the domain in z- and y-directions, respectively, as shown in Fig. 3. Note that the x-direction can be discretized in the same way as the z-direction, but it is unnecessary because of the spherical symmetry condition on the x-z plane (cf. Fig. 1). Therefore, this analysis is only concerned with the z-direction on the x-z plane. After the discretizing in the y-direction, the integral form of Equation (1) can be expressed as a summation:

$$P(r) = \int_{-\infty}^{\infty} f_{\nu} \left(\sqrt{r^2 + y^2} \right) dy = \sum_{j=1}^{n} f_{\nu,j} L_{j},$$
 (2)

where $f_{v,j}$, L_j are soot volume fraction and the path length of the attenuated light in the j-th element, respectively.

For each element (e.g., j) in the y-direction, the light beam of intensity I_j is incident on the medium, and the light beam is then attenuated as it passes through the medium due to extinction (see Fig. 4). The intensity of the transmitted light, I_{j+1} , and the incident light, I_j , is related by a modified form of Bouguer's Law [37,38]:

$$\frac{I_{j+1}}{I_i} = \exp(-\kappa_j \cdot L_j) = \exp\left(-\frac{K_e \cdot f_{v,j}}{\lambda} \cdot L_j\right), \tag{3}$$

where the small particle Mie theory [36] gives the expression of the coefficient κ as

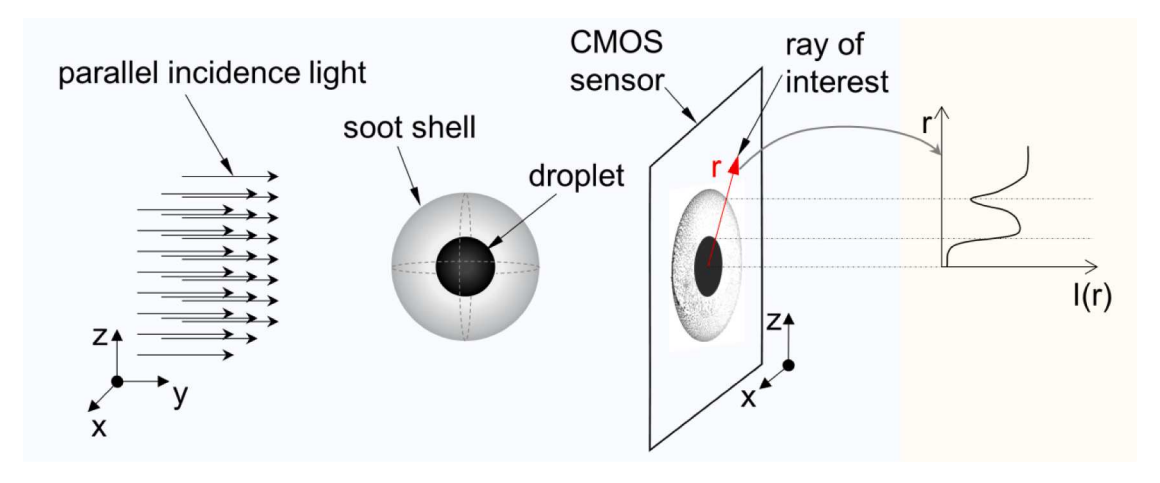


Fig. 1. Schematic of the full-field light extinction method for soot volume fraction measurements.

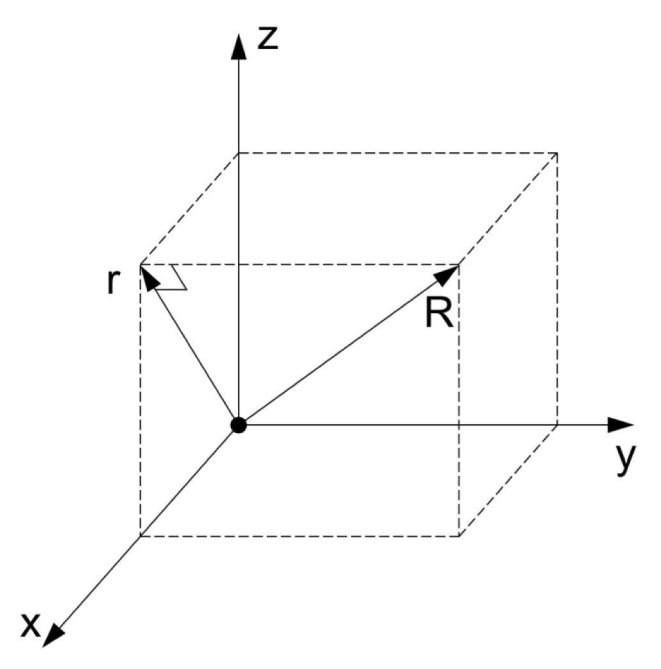


Fig. 2. Schematic of the coordinate system under investigation for f_{ν} measurements.

$$\kappa_j = \frac{K_e f_{v,j}}{\lambda},\tag{4}$$

 λ is the wavelength of the laser light, and K_e is the extinction coefficient [39].

With Equation (3), we can get that

$$f_{v,j}L_j = -\frac{\lambda \ln (I_{j+1}/I_j)}{K_e}$$
 (5)

Plugging Equation (5) into Equation (2) yields

$$P(r) = -\sum_{j=1}^{n} \frac{\lambda \ln \left(I_{j+1} / I_{j} \right)}{K_{e}} = -\frac{\lambda}{K_{e}} \sum_{j=1}^{n} \ln \left(\frac{I_{j+1}}{I_{j}} \right)$$

$$= -\frac{\lambda}{K_{e}} \ln \left(\frac{I_{2}}{I_{1}} \frac{I_{3}}{I_{3}} \dots \frac{I_{n+1}}{I_{n}} \right) = -\frac{\lambda}{K_{e}} \ln \left(\frac{I_{n+1}}{I_{1}} \right).$$
(6)

We use I_0 and I to present the incident light intensity prior to the first element (i.e., $I_1=I_0$ as shown in Fig. 4) and the transmitted light intensity after the last element (i.e., $I_{n+1}=I$ in Fig. 4), respectively. Therefore, Equation (6) can be written as

$$P(r) = -\frac{\lambda \ln (I/I_o)}{K_e}.$$
 (7)

The values of P can be calculated, along with the ROI (i.e., r-direction in Figs. 1 and 2), using Equation (7). In the present study, the ratio of light intensity, I/I_0 , is evaluated from two images: the first image is the background image taken prior to droplet ignition that provides the incident light intensity I_0 , and the second image is a soot-attenuated image recorded during combustion, which gives the transmitted light intensity, I.

With the measured P values, the field values that correspond to the soot volume fraction can be determined using a purely mathematical technique: the three-point Abel inversion technique, as recommended by Dasch [35] for the specific application related to the present study. The field distribution $f_v(r_i)$ can then be found at a finite domain using

$$f_{\nu}(r_i) = \frac{1}{\Delta r} \sum_{k=1}^{m} D_{ik} P(r_k),$$
 (8)

where $r_i = i \cdot \Delta r$ is the radial distance from the center of the droplet on the x-z plane (i.e., on the recorded BW soot-attenuated image), Δr is the data spacing, D_{ik} is the operator coefficients for the three-point Abel inversion [35], $P(r_k)$ is the discretized form of P(r) and is calculated using Equation (8). Note that there are a number of typos in the article (i.e., [35]) that provides D_{ik} , and that the errata can be found in [40].

The tomographic inversion technique based on Equation (8) has been widely used for obtaining quantitative measurements of soot volume fraction in droplet combustion experiments performed under low gravity [18–21]. However, no open-source program is currently available to extract soot volume fraction measurements from consecutive digital images. Moreover, there is no program capable of extracting soot volume fraction when the droplet drifts during combustion, as the droplet in previously reported experiments for such measurements was tethered and thus not free to move [18,20,21]. This work aims to bridge these gaps by developing automated analysis algorithms based on MATLAB to analyze images with both tethered and untethered droplets during combustion, as discussed in the next section.

4. The MATLAB algorithm: analyze_SVF

In the present study, an automated program based on MATLAB is developed to analyze the sooting images and thus quantitatively extract soot volume fraction. This program is termed "analyze_SVF," and it can analyze images of droplets that are both anchored to support fibers (i.e., 'tethered') and free-floating (or 'untethered'). The program can be accessed at https://github.com/yiren6/analyze_svf.git.

The program is designed to automatically find SVF for multiple axes

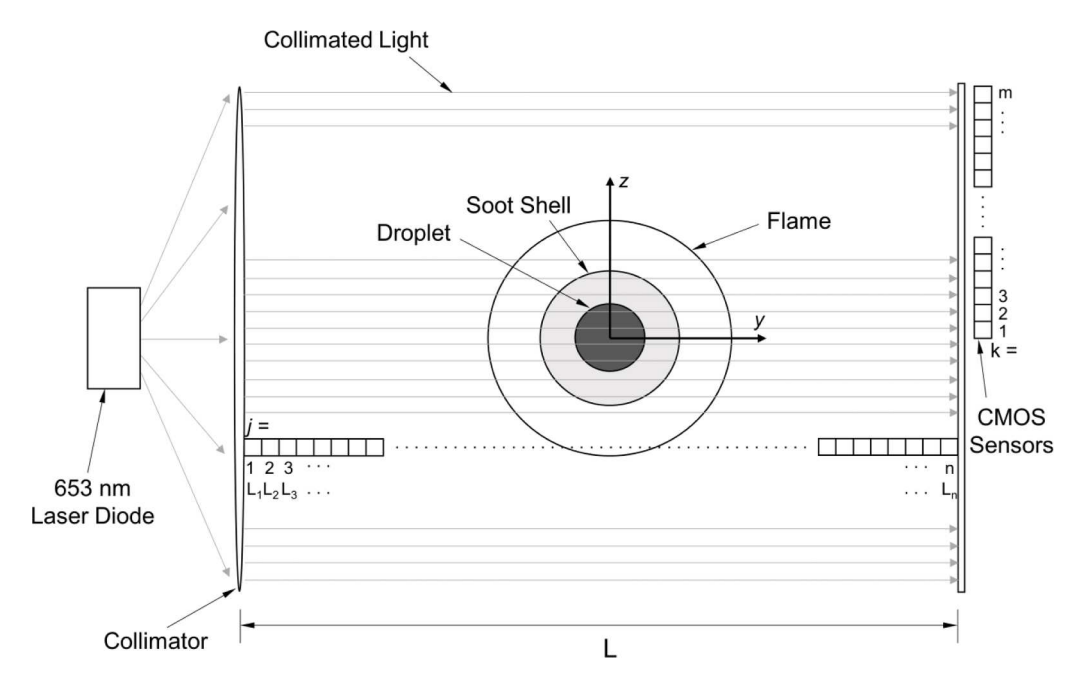


Fig. 3. Illustration of discrete domains in y- and z-directions.

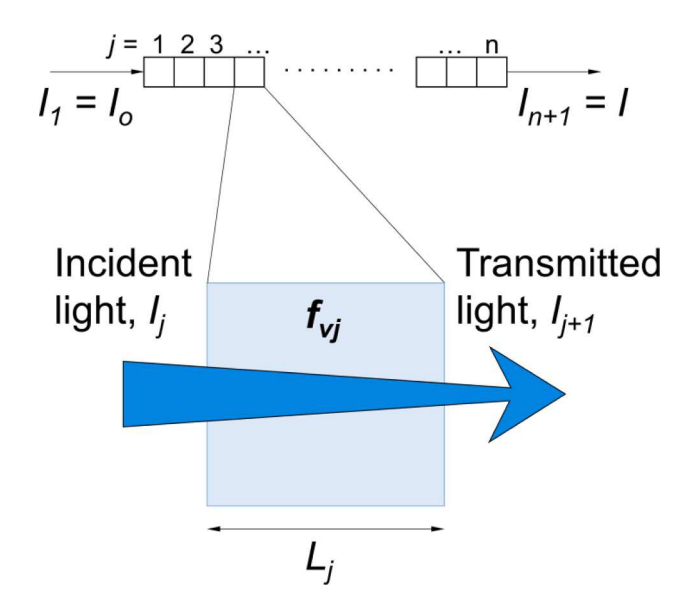


Fig. 4. The attenuation of the light beam in the y-direction while it passes through the j-th element.

(r) within a given region and to accommodate the droplet drifting issue that is common in ISS droplet combustion experiments. The program is designed to use public functions within the image processing toolbox: imfindcircles.m and improfile.m, and the financial toolbox: tsmovavg. m. The program flow chart is described in Fig. 5. The use of the MATLAB programming language developed, based on Fig. 5, is a personal choice of the authors. Other programming languages (e.g., Fortran, C++, Python, etc.) in which to express the algorithm could have been used.

The algorithm prompts the user to load the original and attenuated images. While doing so, the program automatically converts the image to a grayscale intensity matrix with an 8-bit unsigned integer. Since the program adopted a semi-automatic algorithm to identify the droplet center and diameter, the user must manually measure the droplet radius. Such measurements are usually carried out in existing image processing programs [41], and measurements are taken from Ref. [26], which uses ImagePro by Media Cybernetics for image analyses. After obtaining

droplet radius measurements for both images, the user then inputs a potential range of droplet radii, usually at a range of \pm 10 pixels from the manual measurement, to facilitate the program to identify the centers of droplets (in matrix coordinate) and the radii (in pixels) of the droplets for both images. The centers and radii of droplets are then stored and later used to construct ROIs. Two prompt windows for the images will prompt out with the droplet boundary marked in the red circle to help the user verify if the program correctly identifies the droplet. The marked droplet boundary is shown in Fig. 6a.

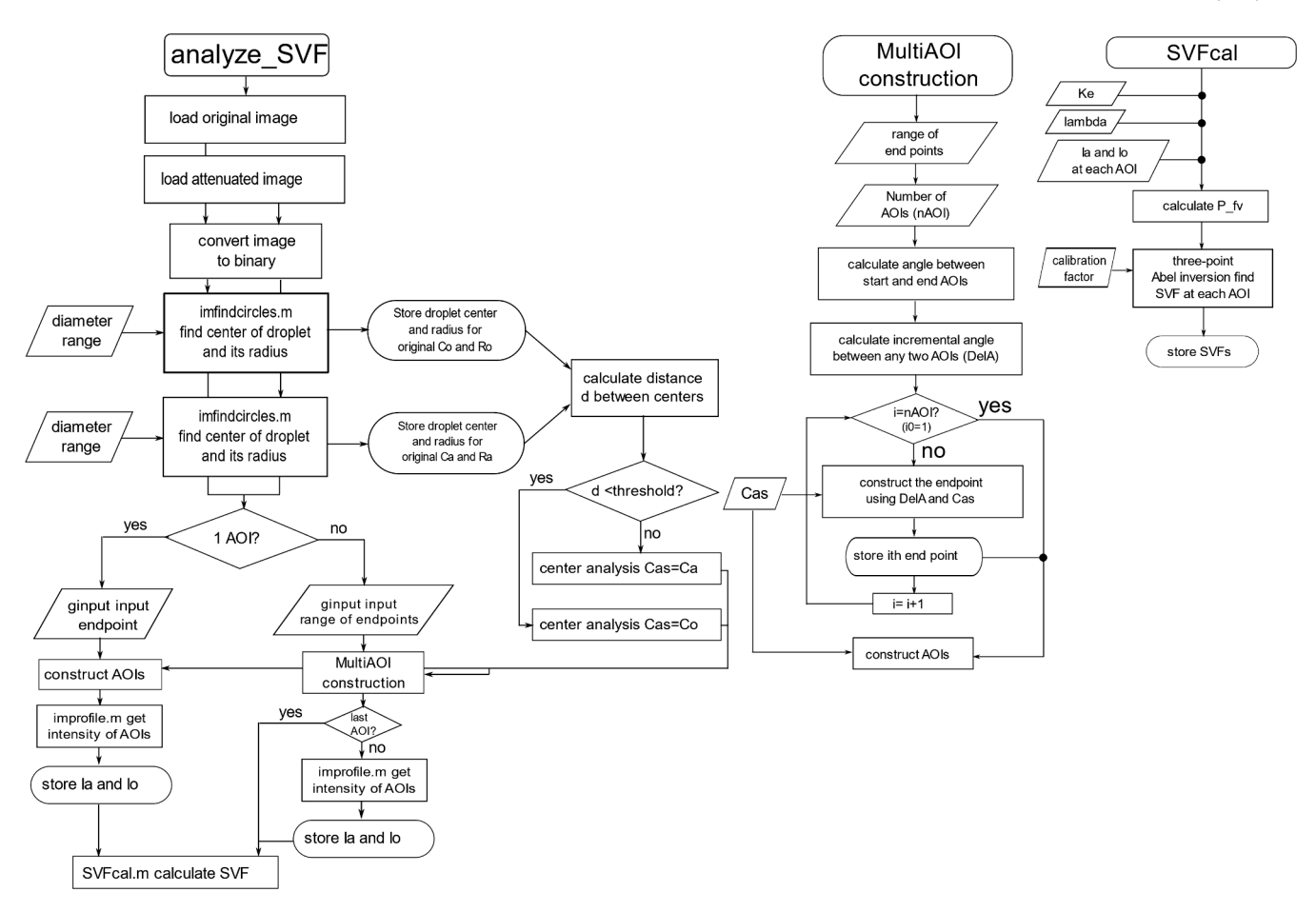
Once the user confirms the droplet selection, the program asks for the number of ROI under investigation. For a single ROI analysis (i.e., $n_{ROI}=1$), the program asks the user to input the endpoint of the ROI using a mouse. For multi-ROI analysis ($n_{ROI}\neq 1$), the user inputs a direction-of-analysis (DOA) angle θ using two mouse inputs, start and end accordingly. Those endpoints are then stored, together with the droplet center that was found in the earlier steps, to construct ROI (or ROIs). As illustrated in Fig. 6b, the first ROI is marked in blue, and the last ROI is marked in red for multiple ROI scenarios. It is worth noting that only the angle marked with θ in the first quadrant is defined by the user, and the counterpart of that angle in the third quadrant is generated automatically by the program.

With the DOA angle defined, the program draws additional ROIs by evenly dividing up the DOA angle so that the angle between any two ROIs on the same quadrant is $\theta/(n_{ROI}$ -1). This process is achieved by constructing endpoints based on the center of the droplet, the radius of the starting ROI, and the position of the starting ROI using basic trigonometry.

Once the ROIs are determined, the program calls for improfile.m to obtain the intensity for both attenuated and original images at each ROI. The intensity profiles are then stored and sent to SVFcal.m to calculate the SVF at each ROI. SVFcal.m uses the tomography inversion technique described previously, which is based on the three-point Abel inversion method. The result is then stored in a matrix and can be exported for future investigation.

5. Results

Selecting appropriate ROIs to extract the measurements of soot volume fraction is very important so that reliable data can be generated from the program "analyze SVF." As discussed previously, both incident



 $\textbf{Fig. 5.} \ \ \textbf{Flow} chart \ for \ the \ analyze_SVF.m \ program \ and \ its \ sub-program.$

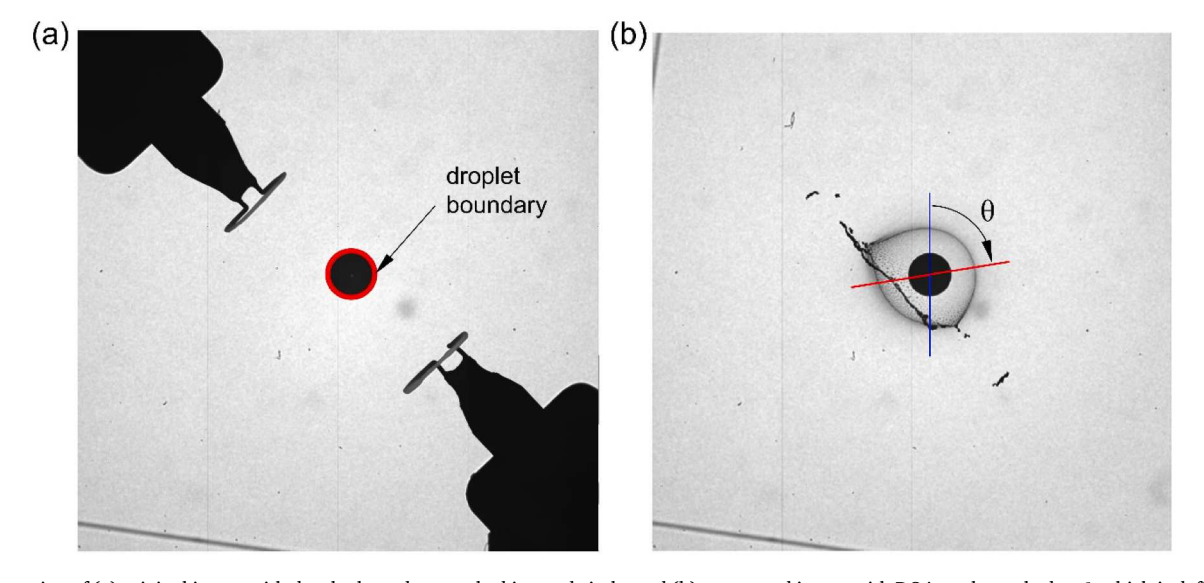


Fig. 6. Illustration of (a) original image with droplet boundary marked in a red circle, and (b) attenuated image with DOA angle marked as θ , which is defined by the user starting from blue ROI and ending with red ROI on the first quadrant.

light intensity from a background image and transmitted light intensity from a soot-attenuated image along the ROIs are needed to perform the calculation. With an ideal spherically symmetric configuration, one can select any ROI as the configuration under investigation is one-dimensional. However, some restrictions do exist that are related to the ISS FLEX-2 experimental setup, including the existence of hot-wire

igniters on the background image and the influence of soot tails formed during combustion on the soot-attenuated image.

Fig. 7 shows an original image for one of the ISS n-heptane ($D_o = 2.63$ mm) test runs. Two hot-wire igniters appear on this image (and all other images with time zero, i.e., prior to ignition, for every ISS test run). As such, there are some directions in which we are unable to extract the

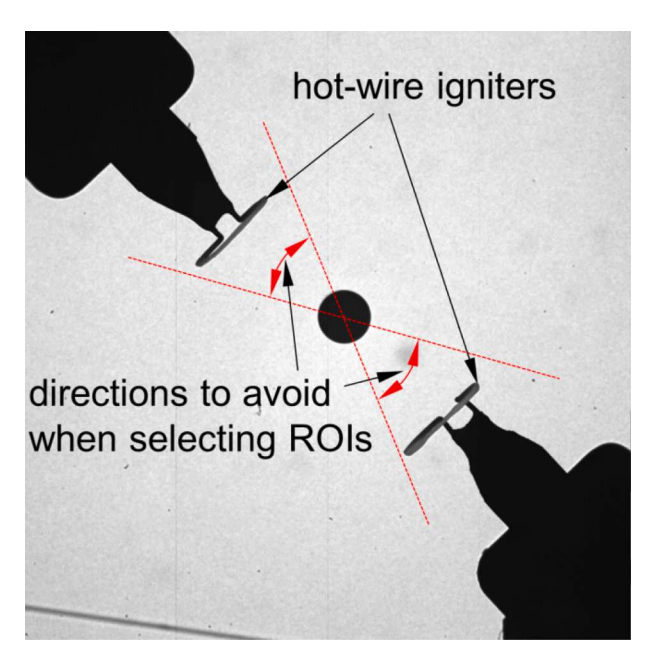


Fig. 7. Illustration of a background image on which hot-wire igniters appear and thus some directions need to be avoided when selecting ROIs.

incident light intensity from such a background image (i.e., the background information is blocked by the two hot-wire igniters). Those directions need to be avoided when selecting ROIs, as shown in Fig. 7.

The other situation in which the ROI needs to be selected carefully involves the effects of large soot aggregates formed during combustion. Fig. 8 shows a soot-attenuated image in which soot aggregates form a tail-like shape, and the soot shell is distorted. The two soot tails shown in Fig. 8 are developed from soot particles formed around igniters during ignition. When the hot-wire igniters are charged, soot particles can form around the igniters. Upon retraction of the igniters, soot particles can be dragged along with the igniters, and a tail-like structure can be formed

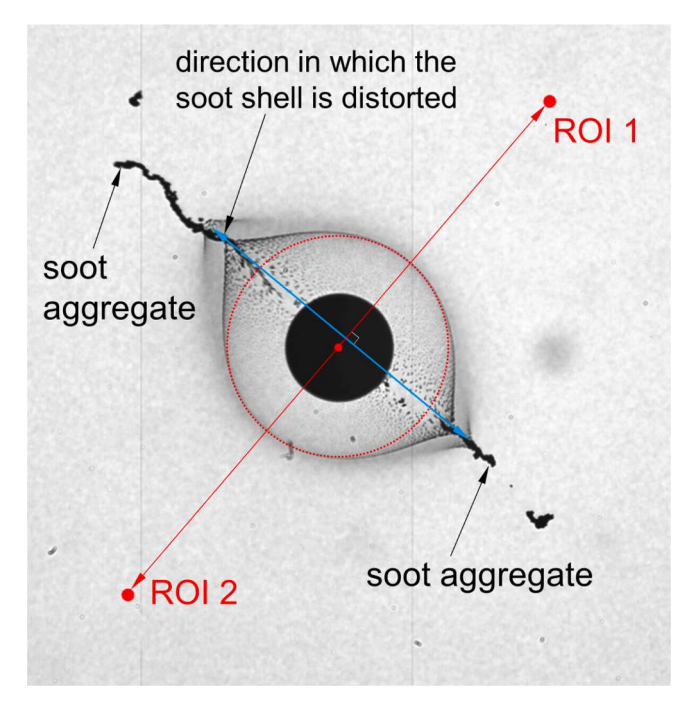


Fig. 8. Illustration of selecting ROIs for a soot-attenuating image (ISS n-heptane test run, $D_o = 3.10$ mm, at $0.25 \, \text{s/mm}^2$) on which soot shell is distorted by soot aggregates. Each ROI starts from the center of the droplet.

when soot particles continue to form and aggregate. With the formation of the soot tail and the dragging effect of hot-wire retraction, the soot shell can be distorted and thus becomes elliptical, as shown in Fig. 8. In this case, the ROI should be selected to pass through the spherical portion of the soot shell (i.e., the portion where the dotted circle overlaps with the soot shell). It is suggested that one should select ROIs along a direction that is perpendicular to the direction in which the soot shell is distorted (see ROIs 1 and 2 in Fig. 8).

Fig. 9 shows the soot volume fraction for ROI 1, ROI 2, and the average profile for the image shown in Fig. 8. The coordinates in Fig. 9 are traditionally used to plot the SVF distributions [20,21]: the x-axis represents the non-dimensional radius (i.e., r/r_d , defined as the spatial radius divided by the radius of the droplet, and $r/r_d = 1$ indicates the position of the droplet surface), and the y-axis represents SVF. The order of magnitude of the soot volume fraction obtained here is usually -6, and thus the SVF is reported in parts per million (ppm) in the present study. As shown in Fig. 9, the profiles for the two ROIs are consistent with each other, and the averaged profile can be easily obtained to illustrate the SVF distribution for the image shown in Fig. 8. It is evident in Fig. 9 that f_v exhibits a peak ($f_{v,max}$) that coincides with the soot shell. The SVF then decreases due to soot oxidation.

In untethered droplet experiments performed onboard the ISS, the influence of the soot aggregate on the soot shell could sometimes be worse than that shown in Fig. 8. Fig. 10 presents a situation in which the soot tail passes through the soot shell in an instant during the burning. As the formation of the soot tail is unwanted, any ROI passing through the soot tail should be avoided. Fig. 11 shows the soot volume fraction profile for six ROIs, among which three of them (i.e., ROIs 1 to 3) are passing through the spherical portion of the soot shell, and the other three (i.e., ROIs 4 to 6) are touching the soot tail, to illustrate the effects of soot tails on the SVF profile.

As shown in Fig. 11a, the f_{ν} profiles for ROIs 4 to 6 have multiple peaks, and the data enclosed by the dotted ellipse result from the ROIs passing through the soot tail structure. These scattering data are purely due to the influence of the ignition and hot-wire retraction, and thus they do not reflect the spherically symmetric configuration of interest. On the other hand, despite the unavoidable asymmetry artifacts induced by hot-wire retraction, it is still possible to make quantitative measurements of f_{ν} for spherically symmetric combustion by manually selecting ROIs that best reflect a spherically symmetric f_{ν} spatial distribution. The f_{ν} profiles for ROIs 1 to 3 in Fig. 11b show such relatively "clean" distributions where only one peak is observed for one ray, and such a peak occurs at the location of a soot shell. Therefore, only data for

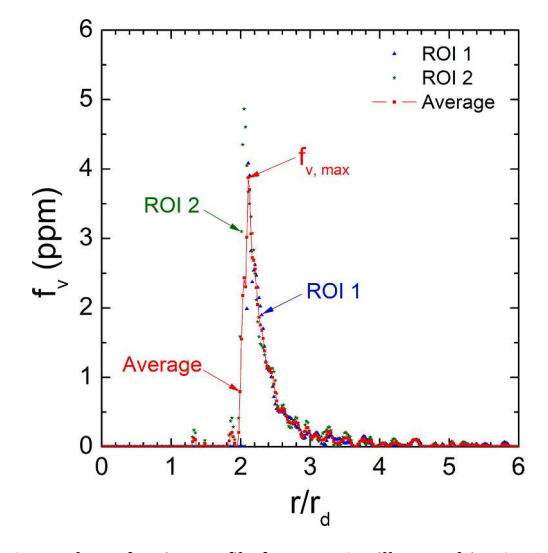


Fig. 9. Soot volume fraction profile for two ROIs illustrated in Fig. 8 and the averaged SVF profile for these two ROIs.

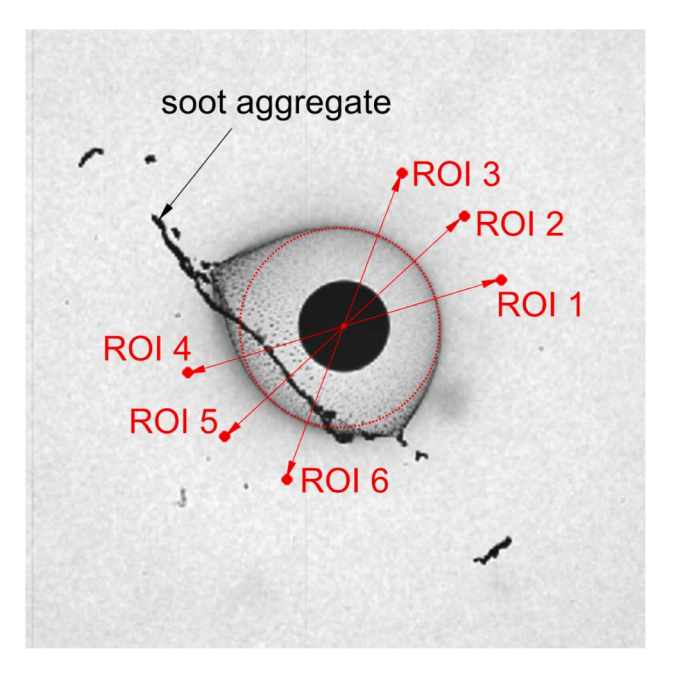


Fig. 10. Illustration of a soot-attenuating image (ISS n-heptane test run, $D_o = 2.63$ mm, at 0.30 s/mm^2) where the soot "tail" passes through the soot shell.

ROIs 1 to 3 should be selected to represent the f_v profile for the image shown in Fig. 10. The f_v shape deviation among ROIs 1 to 3 was quantified using a Pearson correlation test [42]. This test calculated the f_{ν} shape deviation between ROI 1 and ROI 2, which represents the central ROI intersecting the soot shell at the most spherically symmetric location, as well as the deviation between ROI 3 and ROI 2. The Pearson correlation coefficients for the f_v shape deviation were reported as 0.996 for ROI 1 to ROI 2 and 0.958 for ROI 3 to ROI 2. A Pearson correlation coefficient close to 1 indicates an identical shape. In this case, both ROI 1 and ROI 3 had values close to 1, indicating strong shape similarity among ROIs 1 to 3. Therefore, the approach of extracting f_v from a relatively symmetric ROI, as demonstrated by the azimuthal angle between ROI 1 and ROI 3, is valid for reconstructing f_{ν} measurement in spherically symmetric droplet combustion under minor perturbations. The averaged f_{ν} profile obtained using ROIs 1 to 3 is also plotted in Fig. 11b. From the averaged profile in Fig. 11b, the maximum soot volume fraction can be obtained for the instant depicted in Fig. 10. The standard deviation of the difference between the f_{ν} profiles obtained using ROIs 1 to 3 and the averaged f_{ν} profile is 0.0412 ppm, representing

a 0.432% spreading of the maximum average f_{ν} . This small deviation further supports our approach of using ROIs to extract f_{ν} for spherically symmetric droplet combustion.

To validate results obtained by the "analyze_SVF" program, SVF analyses are performed on one previously published image using the program developed in this work, and the results are compared with those obtained using the procedures developed previously that focused on tethered (vs. untethered in this work) droplets [24,43]. For tethered droplets, the feature of tracking the position from prior work was not required. The reference results (i.e., from methods using the previous solver [24,43]) are obtained by running a customized analysis function add-on in Matrox Inspector 8.0 for a prescribed ROI. The current results are obtained by running "analyze_SVF" developed in this work for the same image and ROI. Since the "analyze SVF" program tracks the position of a droplet, it automatically applies also to tethered droplets where the position of the droplet will not change. The comparisons of these results are shown in Fig. 12. It is clear that the results demonstrated a good match between the two methods, with an average absolute discrepancy of 0.347 ppm, corresponding to 1.50% of maximum SVF. To quantify the slight shape difference between the current and reference measurements, the Pearson correlation coefficient [42], $\rho_{\rm p}$, is calculated. The resulting ρ_p is 0.989, indicating an almost identical tracking for the measurements by the current program and reference methodology. These results provide evidence for the accuracy and reliability of the "analyze_SVF" program, highlighting its potential for quantifying sooting dynamics using FFLEM analyses.

Furthermore, a Monte Carlo (MC) measurement is carried out to quantify the uncertainty of measurements by perturbing the ROI in a small region for one attenuated image [44]. According to the FFLEM field distribution assumption, the field distribution is spherically symmetric [35]. Under the limitation of asymmetricity of experimental data, however, the symmetricity of soot is undermined. Selecting ROI on the most spherical region of soot distribution is used instead to extract SVF. However, the selection of ROI is subjective. When two researchers extract SVF using the developed code from this work, they may not select the exact ROIs, despite adhering to a selection criterion of defining ROI at the most spherical region of soot distribution. This induced uncertainty of measurement. Hence, a Monte Carlo measurement around a small azimuthal ROI perturbation quantifies the uncertainty of measurement for potential minor differences in defining ROIs. This study uses attenuated images from the ISS n-heptane test run at initial diameters of $D_0 = 1.59, 1.75, 1.93, 2.27, 2.63, 2.76, 2.88, 3.10, 3.32, and$ 3.55 mm with scaled time t/D_0^2 at 0.2 and 0.3 s/mm² to quantify the uncertainty. The selection of initial diameters covers the entire scope of the analyzable dataset, and the selection of scaled time at 0.2 and 0.3 s/

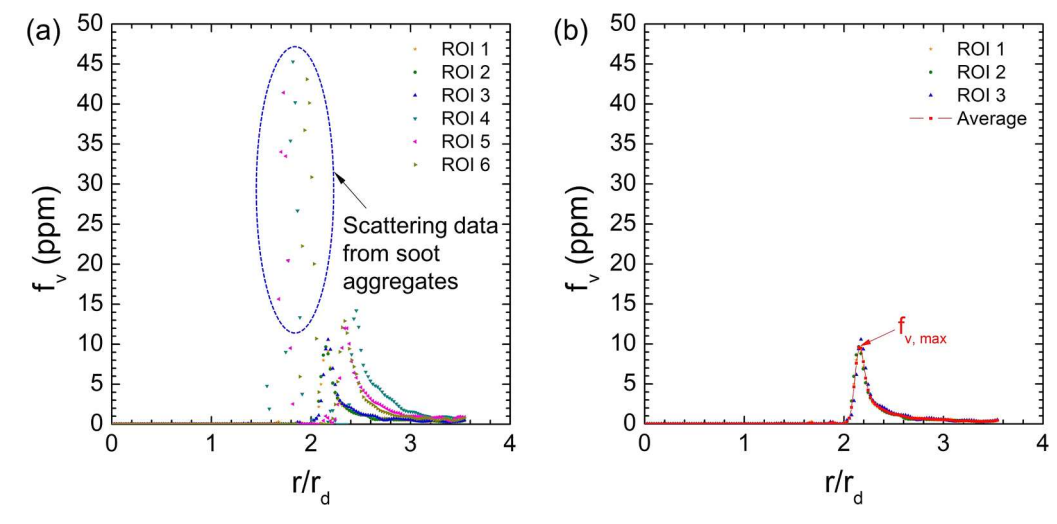


Fig. 11. Soot volume fraction distributions for the image illustrated in Fig. 10: (a) f_v along six ROIs; (b) f_v along three ROIs and their average.

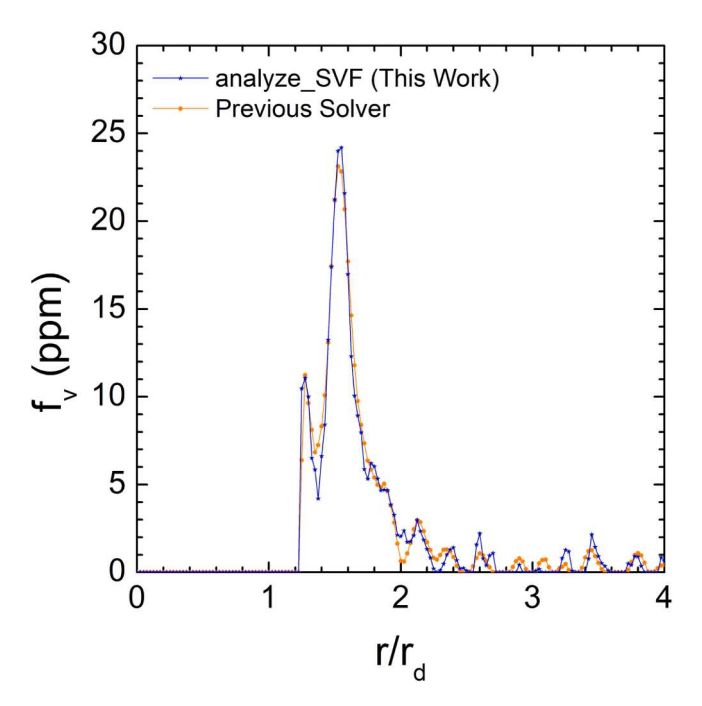


Fig. 12. Comparisons of soot volume fraction measured by the "analyze_SVF" program developed in this work and a previous solver [24,43].

mm² is based on the condition that soot does not form small aggregates while the soot shell has developed enough to enable SVF measurements. The SVF is measured for four ROIs distributed evenly among a 4-degree azimuthal section at the most spherical portion of the soot distribution. The standard deviation of SVF measurements for these four ROIs is then calculated, and the overall average standard deviation is 0.0815 ppm, which should be recognized as the uncertainty of an SVF measurement induced by the ROI definition in this work. Table 1 lists the observed average standard deviation for each individual test run.

The SVF profiles shown in Figs. 9 and 11b are only for one instant in a certain burning event. To investigate the temporal effects on $f_{\nu, \text{max}}$, one should analyze all the images for a particular test run (i.e., one initial droplet diameter) following the protocol discussed previously (see Figs. 7 to 11). We take one n-heptane test run with $D_o = 2.88$ mm to illustrate this process, and Fig. 13 shows the results.

The f_v distributions from 0.10 to 0.50 s/mm² are plotted in Fig. 13a. Each f_v profile in Fig. 13a has a peak value that indicates the maximum soot volume fraction for each instant (i.e., each image). The maximum soot volume fraction is then plotted against the normalized time in Fig. 13b. It is evident that the $f_{v,\text{max}}$ first increases until a peak value is reached (i.e., 14.76 in Fig. 13b) at around 0.35 s/mm², after which $f_{v,\text{max}}$ decreases. Therefore, if one is interested in obtaining the maximum f_v for a particular test run (i.e., one particular D_o), scanning every single image in the test is not required. Alternatively, one should find the trend

Table 1Standard deviation of SVF measurements from perturbed ROIs at a 4-degree azimuthal section.

D_o (mm)	Average Standard Deviation (ppm)	
1.59	0.0854	
1.75	0.0854	
1.93	0.0718	
2.27	0.0601	
2.63	0.0676	
2.76	0.0902	
2.88	0.120	
3.10	0.0765	
3.32	0.1060	
3.55	0.0523	

depicted in Fig. 13b and identify when $f_{\nu, max}$ starts to decrease. As long as a similar trend in Fig. 13b is clearly observed, the scan can then be stopped. For all the n-heptane images analyzed in this study, analyzing images up to 0.5 s/mm² is sufficient to reveal the trend in Fig. 13b and thus identify the $f_{\nu, max}$ for a particular test run.

The trends of the soot volume fraction shown in Figs. 9, 11, and 13 are consistent with previously published results [20,21]. More importantly, the maximum f_v values identified in this study are quantitatively consistent with the previously reported values, considering some influences of the initial droplet diameter [20].

Using the program and protocol discussed above, n-heptane images from ISS experiments reported previously [26] are analyzed to obtain the maximum soot volume fraction for each D_o , and Fig. 14 shows the results. Images for n-heptane are selected here to study the effects of initial droplet sizes on $f_{\nu, \max}$ because the extinction coefficient for n-heptane is known. Furthermore, soot shells for n-heptane images are more intact compared to experimental images of other fuel systems, such as iso-octane [27] and iso-octane iso-octane is-octane is

Fig. 14 shows that $f_{\nu, \rm max}$ decreases with increasing D_o for ISS n-heptane tests (i.e., $D_o > 1.5$ mm). This result is consistent with visual observations of less soot formed and dimmer flame brightness as D_o increases, as shown in Ref. [26]. The trend shown in Fig. 14 is likely to be associated with flame temperature and thus the tendency to form soot. With an increased initial droplet size, the radiative losses from the droplet flames reduce the flame temperature. Consequently, the reduced flame temperature would decrease the tendency to form soot (i.e., limit soot formation), as pyrolysis reactions that produce soot precursors have a more significant temperature dependence than the reactions that attack the soot precursors [45,46].

6. Conclusions

An algorithm has been developed that successfully extracts soot volume fractions from digital images of burning droplets of sooting fuels in an automated manner. The algorithm is based on the full field light extinction method and utilizes the tomography inversion technique, using three-point Abel inversion to quantitatively obtain the soot volume fraction data. This program extends the image analysis capability of the ISS FLEX-2 project and thus enables us to obtain more quantitative data for evaluating the sooting dynamics during liquid fuel combustion.

The proper selection of the ray-of-interests when using the algorithm depends on the nature of the soot-attenuating images being analyzed. One should select ROIs along the direction in which the background intensity is not blocked by the hot wire igniters and the soot shell is not distorted. The program is used to analyze untethered droplets during *n*heptane droplet combustion. The results of the soot volume fraction as a function of a non-dimensional radius show a peak that coincides with the soot shell location. The analysis of the temporal effects on the maximum soot volume fraction shows that SVF_{max} first increases after the burning is initiated until a peak value is reached, after which SVF_{max} decreases. The SVF profiles and SVF_{max} values reported in this work are consistent with previously reported results. The investigations of nheptane tests with different initial droplet sizes indicate that SVF_{max} decreases with increasing initial droplet size, which is consistent with visual observations of less soot formed and dimmer flame brightness as D_o increases reported previously.

CRediT authorship contribution statement

Yuhao Xu: Conceptualization, Methodology, Formal analysis, Investigation, Writing – original draft, Writing – review & editing. Yiren Shen: Software, Formal analysis, Writing – original draft. C. Thomas Avedisian: Conceptualization, Writing – review & editing, Supervision. Michael C. Hicks: Investigation, Supervision, Writing – review & editing, Mun Y. Choi: Resources, Validation.

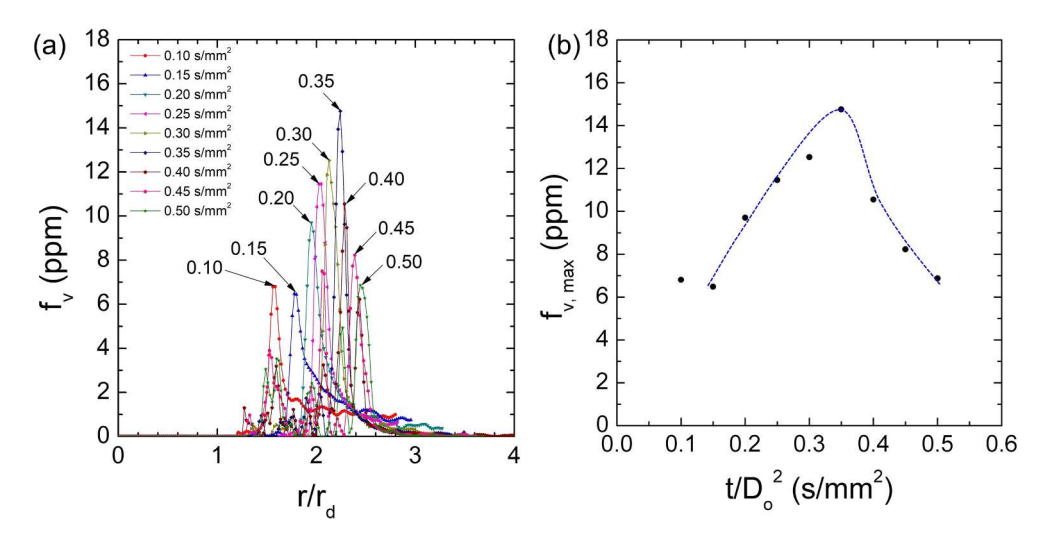


Fig. 13. (a) Soot volume fraction distributions for 0.10 to 0.50 s/mm² in 0.05-s/mm² increments for a heptane droplet with $D_o = 2.88$ mm. The arrows point to $f_{\nu,\text{max}}$ for each time instant. (b) The maximum soot volume fraction obtained in (a) as a function of normalized time. The dotted line indicates the evolution of $f_{\nu,\text{max}}$ as a function of time.

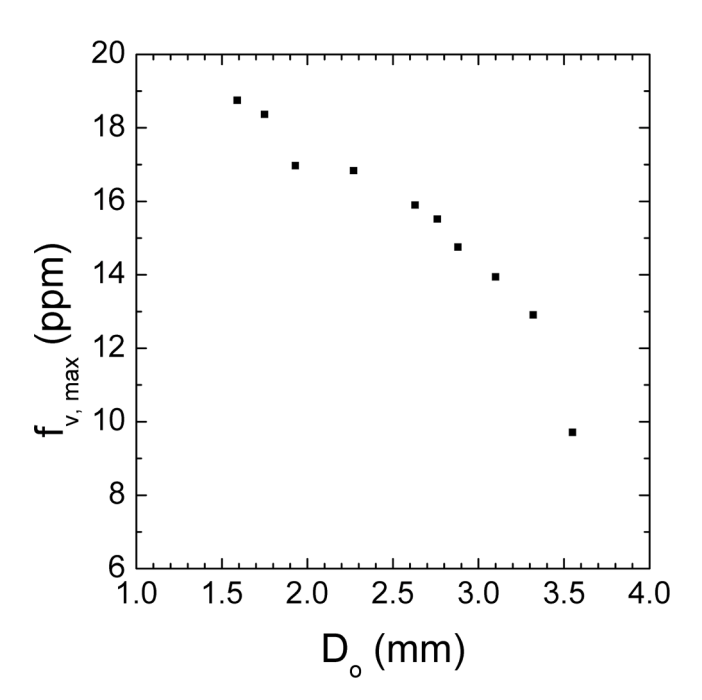


Fig. 14. Dependence of the maximum soot volume fraction on D_o for n-heptane with $D_o>1.5$ mm.

Declaration of Competing Interest

The authors declare that they have no known competing financial interests or personal relationships that could have appeared to influence the work reported in this paper.

Data availability

Data will be made available on request.

Acknowledgments

This research was supported in part by NASA grants NNX08AI51G and #80NSSC18K0480, NSF Grant No. 2055188, and the Office of Energy Efficiency and Renewable Energy's Biotechnology Office of the Department of Energy (DOE) grant no. EE-0007978. Thanks are due to

Drs. John Daily and Harsha Chelliah of NSF and Messrs. Trevor Smith and Robert Natelson of DOE for their interest in our work. The authors also acknowledge discussions with Professor Anthony P. Reeves, Ms. Raisa Rasul, and Mr. Jordan Brunson of Cornell University, and with Dr. Hyun Kyu Suh of Kongju National University in the course of this investigation.

References

- [1] Choi M, Mulholland GW, Hamins A, Kashiwagi T. Comparisons of the soot volume fraction using gravimetric and light extinction techniques. Combust Flame 1995; 102(1):161–9. https://doi.org/10.1016/0010-2180(94)00282-W.
- [2] A Workshop to Identify Research Needs and Impacts in Predictive Simulation for Internal Combustion Engines (PreSICE), https://www1.eere.energy.gov/vehicles andfuels/pdfs/presice_rpt.pdf; 2011 [accessed December 28, 2021].
- [3] Kadota T, Mizutani S, Wu C-Y, Hoshino M. Fuel Droplet Size Measurements in the Combustion Chamber of a Motored SI Engine via Laser Mie Scattering. SAE International; 1990, SAE Techincal Paper 900477.
- [4] Tabata M, Nagao A, Iida Y. Studies of fuel droplets behavior and flame propagation in combustion chamber on S.I. engine using laser 2-D visualization. Int Sym COMODIA 1990;90:179–84. https://www.jsme.or.jp/esd/laboratory/publishing/comodia/comodia/1990/
- [5] Maricq MM, Podsiadlik DH, Brehob DD, Haghgooie M. Particulate Emissions from a Direct-Injection Spark-Ignition (DISI) Engine. SAE International; 1999, SAE Technical Paper 1999-01-1530.
- [6] Zhao F, Lai MC, Harrington DL. Automotive spark-ignited direct-injection gasoline engines. Progr Energy Combust Sci 1999;25(5):437–562. https://doi.org/10.1016/ S0360-1285(99)00004-0.
- [7] Avedisian CT. Developing Surrogates for Liquid Transportation Fuels: The Role of Spherically Symmetric Droplet Combustion. In: Agarwal AK, Pandey A, Gupta AK, Aggarwal SK, Kushari A, editors. Novel Combustion Concepts for Sustainable Energy Development. New Delhi: Springer India; 2014. p. 379–402. https://link. springer.com/chapter/10.1007/978-81-322-2211-8_16.
- [8] Jackson GS, Avedisian CT, Yang JC. Observations of soot during droplet combustion at low gravity: heptane and heptane/monochloroalkane mixtures. Int J Heat Mass Transfer 1992;35(8):2017–33. https://doi.org/10.1016/0017-9310(92)
- [9] Jackson GS, Avedisian CT. The Effect of Iniatil Diameter in Spherically Symmetric Droplet Combustion of Sooting Fuels. Proc R Soc Lond A 1994;446:255–76. https://doi.org/10.1098/rspa.1994.0103.
- [10] Bae JH, Avedisian CT. Soot Emissions from Spherical Droplet Flames for Mixtures of JP8 and Tripropylene Glycol Monomethyl Ether. Environ Sci Technol 2005;39 (20):8008–13. https://doi.org/10.1021/es048516w.
- [11] Bard S, Pagni P. Spatial variation of soot volume fractions in pool fire diffusion flames. Fire Safety Science–Proceedings of the First International Symposium 1985:361-9.
- [12] Ross HD. Microgravity Combustion: Fire in Free Fall. San Diego: Academic Press; 2001. https://doi.org/10.1115/1.1508155.
- [13] Cenker E. Imaging measurements of soot particle size and soot volume fraction with laser-induced incandescence at Diesel engine conditions. EngD, Ecole Centrale Paris 2014, https://nbn-resolving.org/urn:nbn:de:hbz:464-20150107-110750-9.
- [14] Vander Wal RL, Dietrich DL. Laser-induced incandescence applied to droplet combustion. Appl Opt 1995;34(6):1103–7. https://doi.org/10.1364/ AO.34.001103.

- [15] Gupta S, Ni T, Santoro R. Spatial and Time Resolved Soot Volume Fraction Measurements in Methanol/Benzene Droplet Flames. Fall Technical Meeting, The Eastern States Section of the Combustion Institute; 1994, p. 738-43.
- [16] Vander WR. Laser-induced incandescence: excitation and detection conditions, material transformations and calibration. Appl Phys B 2009;96(4):601–11. https://doi.org/10.1007/s00340-009-3521-0.
- [17] Lee K-O. The effects of sooting in droplet combustion under microgravity and normal-gravity conditions. Ph.D., University of Illinois at Chicago, 1997.
- [18] Choi MY, Kyeong-Okk L. Investigation of sooting in microgravity droplet combustion. Symp (Int) Combust 1996;26(1):1243–9. https://doi.org/10.1016/ S0082-0784(96)80341-9.
- [19] Lee K-O, Manzello SL, Choi MY. The Effects of Initial Diameter on Sooting and Burning Behavior of Isolated Droplets under Microgravity Conditions. Combust Sci Technol 1998;132(1-6):139-56. https://doi.org/10.1080/00102209808952013.
- [20] Manzello SL, Choi MY, Kazakov A, Dryer FL, Dobashi R, Hirano T. The burning of large n-heptane droplets in microgravity. Proc Combust Inst 2000;28(1):1079–86. https://doi.org/10.1016/S0082-0784(00)80317-3.
- [21] Manzello SL, Yozgatligil A, Choi MY. An experimental investigation of sootshell formation in microgravity droplet combustion. Int J Heat Mass Transfer 2004;47 (24):5381–5. https://doi.org/10.1016/j.ijheatmasstransfer.2004.07.008.
- [22] Urban BD, Kroenlein K, Kazakov A, Dryer FL, Yozgatligil A, Choi MY, et al. Sooting behavior of ethanol droplet combustion at elevated pressures under microgravity conditions. Microgravity Sci Technol 2004;15(3):12–8. https://doi.org/10.1007/ bf02870060
- [23] Manzello SL, Park S-H, Yozgatligil A, Choi MY. Fuel-dependent effects on droplet burning and sooting behaviors in microgravity. Energy Fuels 2009;23:3586–91. https://doi.org/10.1021/ef900450n.
- [24] Park S-H, Choi MY. Influences of Residence time of Fuel Vapor Transport on Sooting Behavior of Ethanol Droplet Flames in Microgravity. Microgravity Sci Technol 2015;27(5):337–44. https://doi.org/10.1007/s12217-015-9420-6.
- [25] Mathews JH, Fink KD. Numerical Methods Using MATLAB. 4th ed. Pearson; 2004.
- [26] Liu YC, Xu Y, Hicks MC, Avedisian CT. Comprehensive study of initial diameter effects and other observations on convection-free droplet combustion in the standard atmosphere for n-heptane, n-octane, and n-decane. Combust Flame 2016; 171:27–41. https://doi.org/10.1016/j.combustflame.2016.05.013.
- [27] Xu Y, Hicks MC, Avedisian CT. The combustion of iso-octane droplets with initial diameters from 0.5 to 5 mm: Effects on burning rate and flame extinction. Proc Combust Inst 2017;36(2):2541–8. https://doi.org/10.1016/j.proci.2016.07.096.
- [28] Xu Y, Farouk TI, Hicks MC, Avedisian CT. Initial diameter effects on combustion of unsupported equi-volume n-heptane/iso-octane mixture droplets and the transition to cool flame behavior: Experimental observations and detailed numerical modeling. Combust Flame 2020;220:82–91. https://doi.org/10.1016/j. combustflame.2020.06.012.
- [29] Farouk TI, Dryer FL. Isolated n-heptane droplet combustion in microgravity: "Cool Flames" – Two-stage combustion. Combust Flame 2014;161(2):565–81. https:// doi.org/10.1016/j.combustflame.2013.09.011.

- [30] Farouk TI, Xu Y, Avedisian CT, Dryer FL. Combustion characteristics of primary reference fuel (PRF) droplets: Single stage high temperature combustion to multistage "Cool Flame" behavior. Proc Combust Inst 2017;36(2):2585–94. https://doi.org/10.1016/j.proci.2016.07.066.
- [31] Dietrich DL, Nayagam V, Hicks MC, Ferkul PV, Dryer FL, Farouk T, et al. Droplet Combustion Experiments Aboard the International Space Station. Microgravity Sci Technol 2014;26:65–76. https://doi.org/10.1007/s12217-014-9372-2.
- [32] Banu B. Fluids and combustion facility (FCF) and combustion integrated rack (CIR), NASA John H. Glenn Research Center, Payload Accommodations Handbook CIR-DOC-4064; 2008.
- [33] Robbins J, Shinn C. Multi-user droplet combustion apparatus flex2, NASA John H. Glenn Research Center, Reflight Safety Data Package MDC-DOC-1790A; 2010.
- [34] Modest MF. Radiative Heat Transfer. New York: McGraw-Hill; 1993.
- [35] Dasch CJ. One-dimensional tomography: a comparison of Abel, onion-peeling, and filtered backprojection methods. Appl Opt 1992;31(8):1146–52. https://doi.org/10.1364/A0.31.001146.
- [36] Van de Hulst HC. Light Scattering by Small Particles. New York: John Wiley & Sons; 1957.
- [37] Siegel R, Howell JR. Thermal Radiation Heat Transfer. 3rd ed. Washington, D.C.: Hemisphere Publication Corporation; 1992.
- [38] Malinin DR, Yoe JH. Development of the laws of colorimetry: A historical sketch. J Chem Educ 1961;38(3):129. https://doi.org/10.1021/ed038p129.
- [39] Choi MY, Mulholland GW, Hamins A, Kashiwagi T. Comparisons of the soot volume fraction using gravimetric and light extinction techniques. Combust Flame 1995; 102(1–2):161–9. https://doi.org/10.1016/0010-2180(94)00282-W.
- [40] Martin KM. Acoustic modification of sooting combustion. Ph.D., The University of Texas at Austin, 2002.
- [41] Dembia CL, Liu YC, Avedisian CT. Automated data analysis for consecutive images from droplet combustion experiments. Image Anal Stereology 2012;31(3):137–48. https://doi.org/10.5566/ias.v31.p137-148.
- [42] Freedman D, Pisani R, Purves R. Statistics. 4th ed.: W. W. Norton & Company; 2007.
- [43] Park S-H. Graphic User Interface (GUI) based Soot Volume Fraction Measurement Program for Microgravity Droplet Combustion, University of Connecticut, Internal Report Submitted to Professor Mun Young Choi; 2009.
- [44] Wang H, Sheen DA. Combustion kinetic model uncertainty quantification, propagation and minimization. Progr Energy Combust Sci 2015;47:1–31. https://doi.org/10.1016/j.necs.2014.10.002.
- [45] Schug KP, Manheimer-Timnat Y, Yaccarino P, Glassman I. Sooting Behavior of Gaseous Hydrocarbon Diffusion Flames and the Influence of Additives. Combust Sci Technol 1980;22(5–6):235–50. https://doi.org/10.1080/ 00102208008952387.
- [46] Glassman I, Yaccarino P. The temperature effect in sooting diffusion flames. Symp (Int) Combust 1981;18(1):1175–83. https://doi.org/10.1016/S0082-0784(81) 80122-1.